ANNUAL REVIEWS

Annual Review of Analytical Chemistry

Lighting Up Live-Cell and In Vivo Central Carbon Metabolism with Genetically Encoded Fluorescent Sensors

Zhuo Zhang,[1,2] Xiawei Cheng,[1,2] Yuzheng Zhao,[1,2] and Yi Yang[1,3]

[1]Optogenetics and Synthetic Biology Interdisciplinary Research Center, State Key Laboratory of Bioreactor Engineering, Shanghai Collaborative Innovation Center for Biomanufacturing Technology, Research Unit of Chinese Academy of Medical Sciences, East China University of Science and Technology, Shanghai 200237, China; email: yuzhengzhao@ecust.edu.cn, yiyang@ecust.edu.cn

[2]Shanghai Key Laboratory of New Drug Design, School of Pharmacy, East China University of Science and Technology, Shanghai 200237, China

[3]CAS Center for Excellence in Brain Science, Shanghai Institutes for Biological Sciences, Chinese Academy of Sciences, Shanghai 200031, China

Annu. Rev. Anal. Chem. 2020. 13:293–314

First published as a Review in Advance on March 2, 2020

The *Annual Review of Analytical Chemistry* is online at anchem.annualreviews.org

https://doi.org/10.1146/annurev-anchem-091619-091306

Keywords

central carbon metabolism, genetically encoded fluorescent sensors, real-time monitoring, fluorescence imaging

Abstract

As the core component of cell metabolism, central carbon metabolism, consisting of glycolysis, the pentose phosphate pathway, and the tricarboxylic acid cycle converts nutrients into metabolic precursors for biomass and energy to sustain the life of virtually all extant species. The metabolite levels or distributions in central carbon metabolism often change dynamically with cell fates, development, and disease progression. However, traditional biochemical methods require cell lysis, making it challenging to obtain spatiotemporal information about metabolites in living cells and in vivo. Genetically encoded fluorescent sensors allow the rapid, sensitive, specific, and real-time readout of metabolite dynamics in living organisms, thereby offering the potential to fill the gap in current techniques. In this review,

we introduce recent progress made in the development of genetically encoded fluorescent sensors for central carbon metabolism and discuss their advantages, disadvantages, and applications. Moreover, several future directions of metabolite sensors are also proposed.

1. INTRODUCTION

Central carbon metabolism, including the glycolytic pathway, the pentose phosphate pathway, and the tricarboxylic acid (TCA) cycle, is the core of cell metabolism (**Figure 1**). These metabolic pathways catabolize some of the most important nutrients, glucose and other sugars, then either feed the mitochondrial respiratory chain with reducing equivalents for energy production or accumulate various building blocks for biomass synthesis. Meanwhile, the reducing equivalents produced from central carbon metabolism play a major role in redox homeostasis. Owing to its fundamental importance, central carbon metabolism is weaved into a large number of physiologic or pathological processes of cells and organisms, ranging from embryonic development to aging

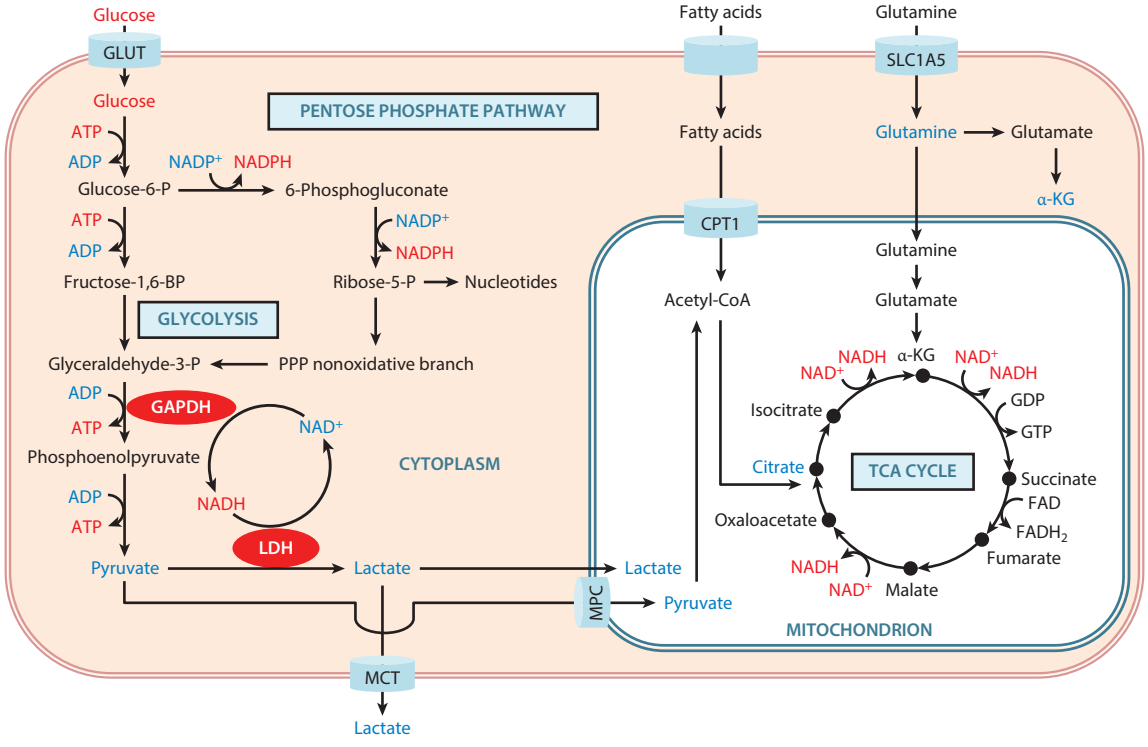

Figure 1

Overview of central carbon metabolism. Abbreviations: α-KG, α-ketoglutarate; CPT1, carnitine palmitoyltransferase 1; Fructose-1,6-BP, fructose 1,6-bisphosphate; GAPDH, glyceraldehyde-3-phosphate dehydrogenase; Glucose-6-P, glucose-6-phosphate; GLUT, glucose transporter; Glyceraldehyde-3-P, glyceraldehyde-3-phosphate; LDH, lactate dehydrogenase; MCT, monocarboxylate transporter; MPC, mitochondrial pyruvate carrier; PPP, pentose phosphate pathway; Ribose-5-P, ribose-5-phosphate; SLC1A5, solute carrier family 1 member 5; TCA, tricarboxylic acid.

(1, 2), immune responses to immunological diseases (3, 4), neural activity to nervous system disease (5, 6), nutrient catabolism to metabolic disease (7, 8), and cell proliferation to cancers (9, 10).

In the glycolytic pathway, glucose is first phosphorylated into glucose-6-phosphate and then yields glyceraldehyde-3-phosphate and subsequently pyruvate (**Figure 1**). Pyruvate is transported into mitochondria or reduced into lactate via lactate dehydrogenase. Pyruvate is a major nutrient for early embryo development (1) and lactate is essential for the energy-consuming brain (11). The ratio of pyruvate and lactate is generally balanced with that of NAD^+ and NADH in the cytosol. As the universal energy currency, ATP generated from glycolysis crucially sustains the energy charge of cells, especially when mitochondrial function is impaired. In addition, glyceraldehyde-3-phosphate is the precursor of several important metabolites such as serine and glycerol (12). Phosphoenolpyruvate and pyruvate can generate oxaloacetate and malate through anaplerotic pathways.

The pentose phosphate pathway is an alternative catabolic reaction of glucose, through which glucose can produce phosphorylated ribose and NADPH (**Figure 1**). Ribose is a constitutive composition of several fundamental metabolites, including DNA, RNA, ATP, and coenzyme A, whereas NADPH supplies the ultimate reducing power for both biosynthesis and antioxidant functions (13).

The TCA or Krebs cycle is a series of chemical reactions used by all aerobic organisms to release stored energy that produce reducing equivalents (i.e., NADH, NADPH) and energy currency (ATP and GTP) through the oxidation of acetyl-CoA derived from glucose, fatty acids, and amino acids (**Figure 1**). The intermediate metabolites from the TCA cycle are also precursors of diverse biosynthetic reactions. For example, citrate can transport from mitochondria to cytosol and support fatty acid synthesis; α-ketoglutarate (α-KG) involves the regulation of some protein activities such as those of α-KG-dependent dioxygenases and hydroxylases, which is vital for cell signaling and epigenetic modifications (14); succinate is the substrate for succinylation of proteins and also acts as an inflammatory messenger (15); and malate promotes glycogenesis and also provides an important source for NADPH generation. Therefore, the TCA cycle is a metabolic hub that exerts multiple functions, and its functional deficiency often underlies the development of illness. Prevailing mutations at loci encoding isocitrate dehydrogenase and fumarate hydratase lead to the buildup of 2-hydroxyglutarate (2-HG) (16) and fumarate (17), respectively, which promotes malignant transformation. Glutamine and glutamate, two of the most abundant amino acids in cells, can metabolize into α-KG via glutaminase and glutamate dehydrogenase. Cancer cells frequently utilize glutaminolysis to support their rapid growth and redox homeostasis (18).

As the most common metabolic pathway for cells, central carbon metabolism also exhibits high heterogeneity and dynamics, and their metabolites often change dynamically with developmental stage (1), tissue and cell types (3), and the microenvironmental supply of nutrients and oxygen (19). More importantly, the differential metabolic rates of central carbon metabolism lead to different consequences. For example, we recently showed that the different glycolytic activity confers leukemia-initiating cells with different tumor-initializing ability (20). Thus, the huge diversity of central carbon metabolism requires sensitive and spatiotemporal resolution technologies for metabolic monitoring and imaging.

In this review, we begin by providing a brief overview on traditional biochemical methods and autofluorescence imaging for metabolite measurement in central carbon metabolism, and then give an introduction to the principle, design and optimization of genetically encoded metabolite sensors. Lastly, we focus mainly on recent advances and future perspectives in the development of central carbon metabolism-related biosensors.

2. TRADITIONAL METHODS FOR METABOLITE MEASUREMENT IN CENTRAL CARBON METABOLISM

2.1. Biochemical Methods for Metabolite Measurement

Compared to DNA, RNA, or protein, the metabolome is more difficult to detect, owing to highly diverse structures, instability, large variations of subcellular distribution, and inability to conduct in vitro amplification of samples (21). Conventional biochemical methods, including enzymatic cycling assays (22), chromatography (23), mass spectrometry (24), nuclear magnetic resonance (25, 26), capillary electrophoresis (27, 28), and isotope labeling techniques (29), are often used to measure metabolite levels (30, 31). Recently, metabolomic analyses became popular for quantitating the entire spectrum of metabolites in biological samples to assess the global metabolic state or perturbations (32). However, these methods require sample destruction, provide only static information about a population of cells, and do not capture the transient metabolite changes associated with metabolic activation or dysfunction. Most importantly, these methods are time intensive and incompatible with studying spatiotemporal dynamics in single, intact cells and therefore are not suitable for quantitative, real-time, high-throughput screening of living cells. Coherent anti-Stokes Raman scattering (CARS) or stimulated Raman scattering (SRS) imaging does not require labeling with specific probes and can obtain in situ information about some metabolites such as lipids and starches in living cells. However, it is difficult to monitor the metabolites with relatively small abundance with CARS and SRS because of their low signal-to-noise ratio. In addition, sophisticated imaging instruments are also needed.

2.2. Autofluorescence for Metabolite Measurement

Nicotinamide adenine dinucleotide NAD(H) and its phosphorylated form NADP(H) are important coenzymes found in all living cells and play central roles in central carbon metabolism (**Figure 2**). More than 700 oxidoreductive enzymes use NADH or NADPH as cofactors (33). NADH is produced during glycolysis in the cytosol and via the TCA cycle in the mitochondria and then oxidized by the mitochondrial respiratory chain for ATP production. NADPH is generally thought to be generated primarily via the oxidative pentose phosphate pathway (34). However, there are also other potential sources of NADPH in mammalian cells, including reactions catalyzed by isocitrate dehydrogenase, malic enzyme, methylene tetrahydrofolate dehydrogenase, and nicotinamide nucleotide transhydrogenase (35) (**Figure 2**). NADH and NADPH are weakly fluorescent under ultraviolet excitation [excitation wavelength/emission wavelength (Ex/Em) 350 nm/460 nm]; in contrast, their oxidized counterparts NAD^+ and $NADP^+$ are not (36, 37). Based on its optical property, the weak endogenous fluorescence of NADPH has been studied by single-photon or multiphoton excitation to monitor metabolic states in living cells or in vivo (6, 36, 38) for many years. Researchers have also expanded the application of NADH fluorescence to various experimental samples and conditions, including isolated mitochondria, intact cells, tissue slices, and animal organs (36, 39). Although NAD(P)H autofluorescence has been widely employed, it is limited by low sensitivity and cell injury caused by ultraviolet irradiation. Additionally, as most of the intrinsic NAD(P)H fluorescence originates from the mitochondria, it is difficult to separate and detect cytosolic signals from the bright mitochondrial signals. Even worse, it is difficult to distinguish NADH and NADPH due to their similar fluorescence emission spectrum. Blacker et al. (40) reported that fluorescence lifetime imaging (FLIM) could differentiate NADPH from NADH on the basis of a simple assumption that bound NADH and bound NADPH possess different fluorescence lifetimes inside the cell; however, FLIM is not technically simple for broad applications.

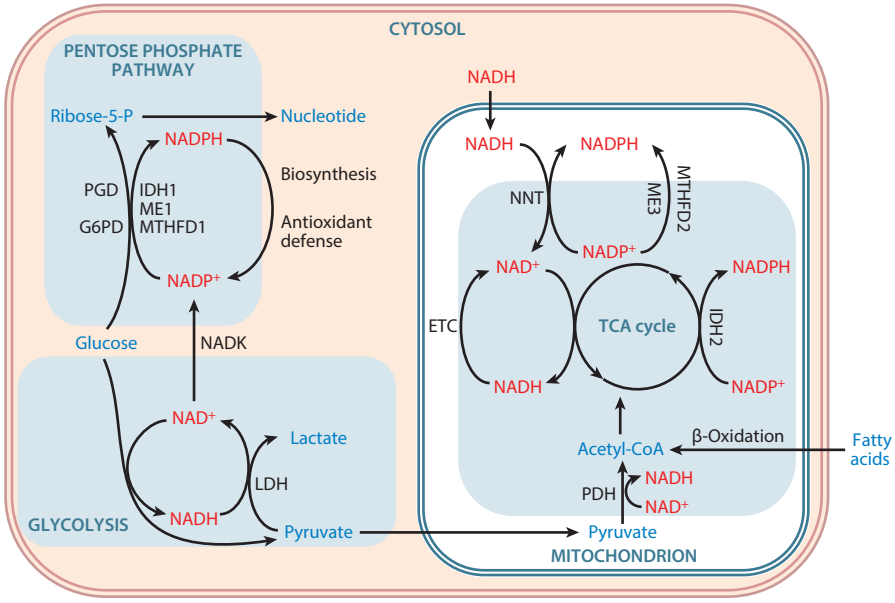

Figure 2

The central roles of NAD^+/NADH and $NADP^+$/NADPH in central carbon metabolism. Abbreviations: ETC, electron transport chain; G6PD, glucose-6-phosphate dehydrogenase; IDH1/2, isocitrate dehydrogenase 1/2; LDH, lactate dehydrogenase; ME1/3, malic enzyme 1/3; MTHFD1/2, methylenetetrahydrofolate dehydrogenase 1/2; NADK, NAD^+ kinase; NNT, nicotinamide nucleotide transhydrogenase; PDH, pyruvate dehydrogenase; PGD, phosphogluconate dehydrogenase; Ribose-5-P, ribose-5-phosphate; TCA, tricarboxylic acid.

Complementary to measuring NAD(P)H fluorescence, cellular metabolic states can also be examined by determining the intrinsic flavin adenine dinucleotide (FAD) fluorescence (Ex/Em 450 nm/520 nm) depending on its oxidation-reduction state (41–43). However, measuring FAD fluorescence was not as popular as monitoring NAD(P)H in metabolic studies due to lower signal and concerns of interference from hemoglobin absorbance (36, 39, 44). Therefore, NAD(P)H autofluorescence monitoring is preferred in blood-perfused organs (36, 39). Unlike NAD(P)H or FAD, the great majority of metabolites in central carbon metabolism lack intrinsic fluorescence, which hinders their direct imaging in living cells and in vivo. Therefore, in situ assay methods with high spatiotemporal resolution are highly desirable for monitoring (sub)cellular metabolite dynamics.

3. PRINCIPLE, DESIGN, AND OPTIMIZATION OF GENETICALLY ENCODED FLUORESCENT SENSORS

Fluorescent proteins (FPs) are widely used in many research fields, for example to track (sub)cellular localization of proteins and report gene expression activity (45). FPs can be also engineered to develop a sensor for real-time imaging of cellular events or activities (46–48). As they are genetically encoded proteins and self-sufficient to form intrinsic fluorophores without an extraneous chemical, it is possible to target these sensors to specific types of cells or even different subcellular organelles via signal peptides, thus allowing accurate spatiotemporal imaging of live-cell metabolic activities. To monitor intracellular events, researchers have developed over

200 genetically encoded biosensors for cellular metabolites, messengers, and conditions over the past two decades (49). These biosensors generally consist of two basic modules: substrate-binding proteins and FPs. From bacteria to mammals, various regulatory proteins and transcription factors specifically sense intracellular biomolecules. The binding of biomolecules to the substrate-sensing protein often triggers conformational changes, which is transferred to the fused FP and affects the fluorescence intensity and/or spectra of the FP.

Usually, genetically encoded fluorescent sensors are classified into two categories, namely, Förster (or fluorescence) resonance energy transfer (FRET)–based sensors and single FP-based sensors (**Figure 3*a*,*b***). FRET-based sensors contain both donor and acceptor FPs, and the FRET efficiency between two proteins changes upon substrate binding (50, 51) (**Figure 3*a***). FRET-based sensors usually have a larger size (typically >54 kDa) but a smaller dynamic range (typically 10–150%) (50). For single FP-based sensors (typically >27 kDa), a circular permuted fluorescent protein (cpFP) is usually utilized and inserted into a loop region of a substrate-binding protein or between tandem units of substrate-binding proteins (50) (**Figure 3*b***). In these cpFPs, the original N and C termini are joined with a short peptide linker, and new N and C termini are created around the fluorophore of cpFPs, making its fluorescence highly sensitive to changes in metabolite levels (52–54). Based on these strategies, these sensors were further optimized by screening of the positions of FP insertion in the substrate-binding protein, screening of the linker between the substrate-binding protein and FPs, mutation of amino acid residues around the binding pocket, and truncation of the substrate-binding protein or linkers between protein domains. These help to improve the specificity for the substrate and magnitude of the response of sensors (ideally, a >500% dynamic range) or to fine-tune the substrate binding affinity [ideally, the sensor's dissociation constant (K_d) is equal to cellular free substrate level] of the sensor for use in living cells. In addition, mutagenesis or replacement of FPs is often carried out to improve the folding and maturation of biosensors or to expand the palette (typically, developing blue, green, and red sensors) for multiparametric imaging (50). The fusion manner between substrate-binding proteins and FPs as well as the readout of the fluorescence response are important aspects for sensor design. Steady-state fluorescence intensity, fluorescence lifetime, and fluorescence anisotropy are most commonly used as readouts. Although the measurements of fluorescence lifetime and fluorescence anisotropy are robust, they require sophisticated instrumentation and complicated analyses. The readout of steady-state fluorescence intensity can be either intensiometric or ratiometric. The latter type of sensor contains two separate emission (i.e., FRET-based sensors) or excitation (i.e., cpFP-based sensors) peaks, and its response is defined as the ratio of two fluorescence channels. Ratiometric readouts have the intrinsic advantage of eliminating the interference from the concentration of the sensor proteins. In summary, the main criteria for superior sensors are rapid response (i.e., the GTP sensors GEVALs, with millisecond response time), appropriate affinity (i.e., the NAD^+/NADH ratio sensor SoNar), high specificity (i.e., the NADPH sensor iNap), high responsiveness (i.e., the NAD^+/NADH ratio sensor SoNar, with a 1,500% dynamic range), intense fluorescence (i.e., the NAD^+/NADH ratio sensor SoNar), good photostability (i.e., the NAD^+/NADH ratio sensor SoNar), antijamming performance (i.e., the NAD^+/NADH ratio sensor SoNar), ratiometric readout [i.e., FRET-based or circular permuted yellow fluorescent protein (cpYFP)-based sensors], convenient measurement (i.e., FRET-based or cpFP-based sensors), or expanded palette (i.e., the $NADP^+$ sensor Apollo-$NADP^+$) (**Figure 3*c***).

Up to now, several genetically encoded metabolite sensors have been developed for the detection of central carbon metabolism (**Figure 3*d*,*e***). In general, they fall into four categories: glycolysis-related sensors, TCA cycle–related sensors, pyridine dinucleotide–related sensors, and energy currency–related sensors (**Table 1**, **Figure 3*d***). Next, we introduce their development, strength, weakness, and applications to facilitate the reader's understanding and use.

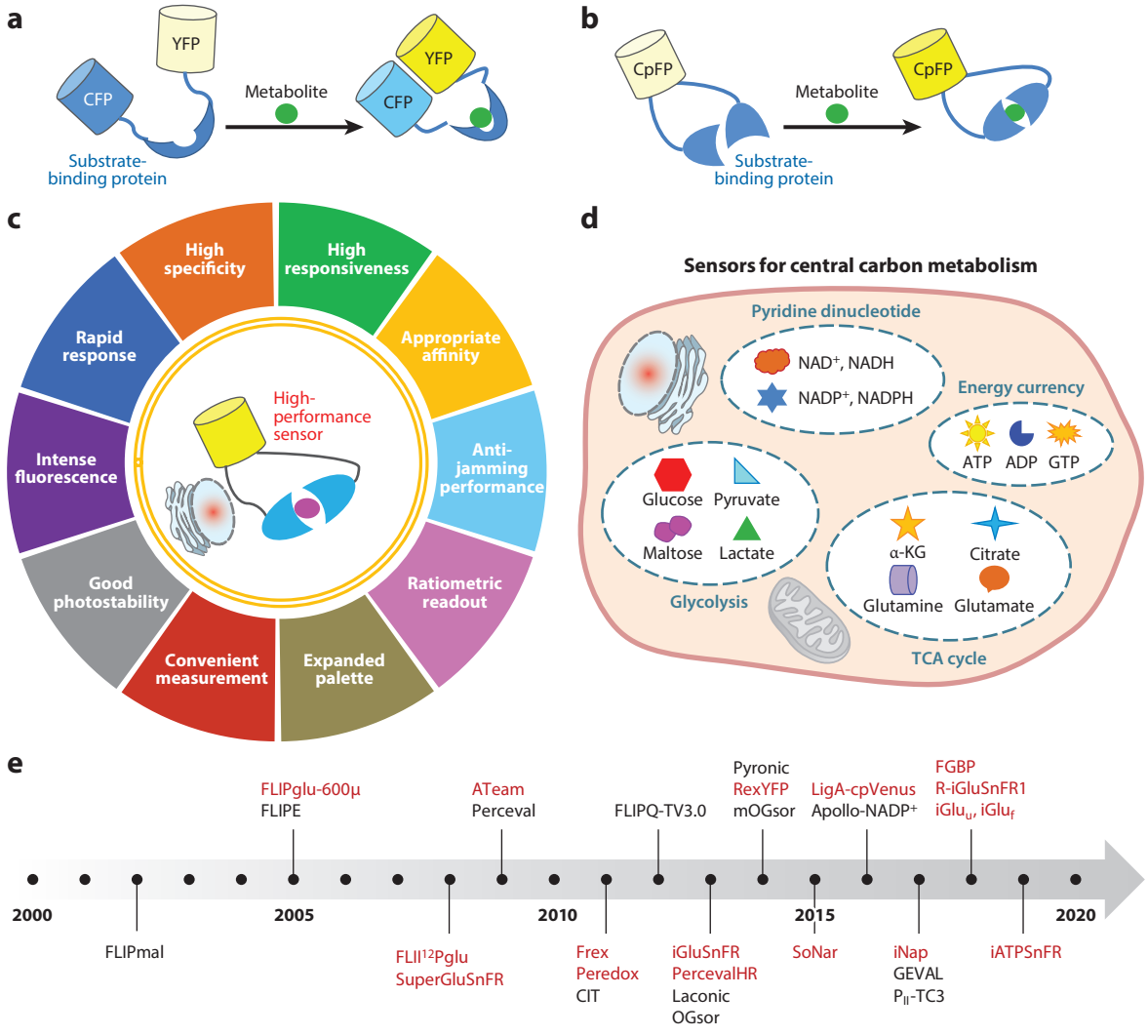

Figure 3

Design and optimization of genetically encoded metabolite sensor. (*a*) FRET-based or (*b*) cpFP-based genetically encoded fluorescent sensors. (*c*) The criteria for superior sensors. (*d*) Historical development of genetically encoded fluorescent sensors in central carbon metabolism. (*e*) Known sensors for central carbon metabolism and dates of development. Sensors with adequate to excellent performance in live cells are shown in red text, and sensors with limited performance and the need of further optimization are shown in black text. Abbreviations: α-KG, α-ketoglutarate; CFP, cyan fluorescent protein; cpFP, circular permuted fluorescent protein; FRET, fluorescence resonance energy transfer; TCA, tricarboxylic acid; YFP, yellow fluorescent protein.

4. GENETICALLY ENCODED FLUORESCENT SENSORS FOR CENTRAL CARBON METABOLISM

4.1. Genetically Encoded Fluorescent Sensors for Glycolysis

For glycolysis, there are currently four types of genetically encoded fluorescent sensors available: the glucose sensors of the FLII^{12}Pglu family and FGBP$_{1mM}$; the maltose sensors of the FLIPmal family, and MBP165-cyan, -blue, -green, and -yellow; the pyruvate sensor Pyronic; and the lactate

Table 1 Fluorescent biosensors for key metabolites of central carbon metabolism

Sensor category	Metabolite sensor	Species sensed	Dynamic changes (%)	K_d or K_R (~ μM)	Detection mode	Reference
Glycolysis	$FLII^{12}Pglu\text{-}600\mu$	Glucose	65	583	FRET	55
	$FLII^{12}Pglu\text{-}10aa$	Glucose	30	1,480	FRET	55
	$FLII^{12}Pglu\text{-}15aa$	Glucose	45	2,650	FRET	55
	$FLII^{12}Pglu\text{-}\delta4$	Glucose	55	600	FRET	55
	$FLII^{12}Pglu\text{-}700\mu\delta6$	Glucose	50	660	FRET	55
	$FGBP_{1mM}$	Glucose	700	1,000	cpYFP	59
	FLIPmal	Maltose	10–20	2.3–226	FRET	60
	Pyronic	Pyruvate	20	107	FRET	62
	Laconic	Lactate	8–10	8, 830	FRET	63
Tricarboxylic acid cycle	CIT	Citrate	20–55	8–1,765	FRET	64
	OGsor	α-Ketoglutarate	10–40	400–2,000	FRET	65
	mOGsor	α-Ketoglutarate	150	ND	FRET	66
	P_{II}-TC3	α-Ketoglutarate	18	3.0	FRET	67
	P_{II}-TC3-R9P	α-Ketoglutarate	ND	91	FRET	67
	FLIPQ-TV3.0_R75K	Glutamine	37	1.5	FRET	69
	FLIPQ-TV3.0_R75M	Glutamine	10	50	FRET	69
	FLIPQ-TV3.0_D157N	Glutamine	35	130	FRET	69
	FLIPQ-TV3.0_R75MY86A	Glutamine	13	1,600	FRET	69
	FLIPQ-TV3.0_ R75MW220A	Glutamine	13	7,600	FRET	69
	FLIPE-600n	Glutamate	27	0.6	FRET	70
	SuperGluSnFR	Glutamate	44	2.5	FRET	71
	iGluSnFR	Glutamate	450	107	FRET	73
	$iGlu_f$	Glutamate	300	137	FRET	74
	$iGlu_u$	Glutamate	280	600	FRET	74
	R-iGluSnFR1	Glutamate	490	11	FRET	75
	R^{ncp}-iGluSnFR1	Glutamate	480	0.9	FRET	75

(*Continued*)

Table 1 (*Continued*)

Sensor category	Metabolite sensor	Species sensed	Dynamic changes (%)	K_d or K_R (~ μM)	Detection mode	Reference
Pyridine dinucleotide	Frex	NADH	800	3.7, 11[a]	cpYFP	76
	LigA-cpVenus	NAD^+	100	65	cpFP	79
	Peredox	NAD^+/NADH ratio	150	330[b]	cpFP	80
	RexYFP	NAD^+/NADH ratio	50	ND	cpYFP	82
	SoNar	NAD^+/NADH ratio	1,500	40[b]	cpYFP	81
	iNap1	NADPH	900	2.0	cpYFP	86
	iNap2	NADPH	1,000	6.0	cpYFP	86
	iNap3	NADPH	900	25	cpYFP	86
	iNap4	NADPH	500	120	cpYFP	86
	Apollo-$NADP^+$	$NADP^+$	15–20	0.1–20	FP	87
	NADPsor	$NADP^+$	30	2,000	FRET	88
Energy currency	AT3.01	ATP	100	7.4	FRET	89
	$AT3.01^{MGK}$	ATP	ND	14	FRET	89
	AT1.03	ATP	150	3,300	FRET	89
	$AT1.03^{YEMK}$	ATP	ND	1,200	FRET	89
	AT1.03NL	ATP	90	1,770	FRET	90
	iATPSnFRs	ATP	190–240	50–120	cpFP	93
	ADPrime	ADP	8.0	0.16	FRET	94
	Perceval	ATP/ADP ratio	80	0.5[c]	cpFP	95
	PercevalHR	ATP/ADP ratio	400	3.5[c]	cpFP	96
	GEVAL530	GTP	130	528	cpYFP	98
	GEVAL1150	GTP	90	1,130	cpYFP	98

[a]The apparent K_d of Frex is ~3.7 μM at pH 7.4 and ~11 μM at pH 8.0.
[b]The apparent K_R (analogous to K_d) for NAD^+/NADH ratio at which the response is half-maximal.
[c]The apparent K_R (analogous to K_d) for ADP/ATP ratio at which the response is half-maximal.
Abbreviations: cpYFP, circular permuted yellow fluorescent protein; FRET, Förster (or fluorescence) resonance energy transfer; K_d, dissociation constant; K_R, half-maximal signal change; ND, not determined.

sensor Laconic (**Table 1**). The characteristics and application of these sensors are each described in the following sections.

4.1.1. Genetically encoded glucose sensors. A series of genetically encoded glucose sensors ($FLII^{12}Pglu$) were constructed by inserting the *Escherichia coli* glucose/galactose-binding protein MglB into a FRET pair (ECFP/citrine-EYFP) (55). The $FLII^{12}Pglu$ sensors are modified versions of the original glucose sensor FLIPglu-600μ (56) and have five variants ($FLII^{12}Pglu$-600μ, $FLII^{12}Pglu$-10aa, $FLII^{12}Pglu$-15aa, $FLII^{12}Pglu$-δ4, and $FLII^{12}Pglu$-700μδ6), whose K_d for glucose ranges from ∼0.6 to ∼2.65 mM in vitro. Upon glucose binding, the ratios of $FLII^{12}Pglu$ sensors change by 30–65%. Compared to the original sensor FLIPglu-600μ, $FLII^{12}Pglu$-700μδ6 has a higher ratio change (50%) and a wider detection range (0.05–9.6 mM) for glucose (55). These glucose sensors have been used for the real-time monitoring of glucose dynamics in yeast and mammalian cells (57, 58). We recently developed a highly responsive, cpYFP-based glucose sensor, $FGBP_{1mM}$, which displays an ∼700% fluorescence change in vitro, almost tenfold greater than that of FRET-based glucose sensors (59). We used the $FGBP_{1mM}$ sensor to monitor glucose transport in living *E. coli* cells and found that the cells took up glucose within 10 min to maintain physiological glucose levels (59).

4.1.2. Genetically encoded maltose sensors. A series of genetically encoded maltose sensors called FLIPmal were constructed by inserting the maltose-binding protein (MBP) into a FRET pair (ECFP/EYFP) (60). The FLIPmal sensors have a small dynamic range (10–20%) and three variants (FLIPmal-2μ, FLIPmal-25μ, and FLIPmal-225μ), whose K_d for maltose ranges from ∼2.3 μM to ∼226 μM in vitro. Notably, FLIPmal sensors' specificity responds to maltose but not to pentoses, hexoses, sugar alcohols, disaccharides, or trisaccharides. To improve the dynamic response and expand the palette, Marvin et al. (61) developed single-wavelength, multicolor maltose sensors by insertion of circularly permuted fluorescent proteins (cpCFPs; cpAzurite, cpGFP, or cpYFP) into a bacterial periplasmic binding protein. The four-colored maltose sensors MBP165-cyan, -blue, -green, and -yellow have different affinities with a K_d of ∼1.7 mM, ∼2.7 μM, ∼40 μM, and ∼350 μM, respectively, and their fluorescence response to maltose ranges from 20% to 250%. These sensors have been used to monitor the maltose uptake across the plasma membrane in living yeast cells (60) or the addition of maltose to extracellular media in HEK293 cells (61).

4.1.3. Genetically encoded pyruvate sensors. A genetically encoded pyruvate sensor named Pyronic was developed by inserting the *E. coli* transcriptional regulator PdhR into a FRET pair (monomeric teal fluorescent protein, mTFP/Venus) (62). The Pyronic sensor responds to pyruvate between 10 μM and 1 mM, with a K_d of ∼107 μM and a dynamic range of ∼20%. This sensor has high specificity and pH resistance. San Martín et al. (62) demonstrated that the Pyronic not only reported cytosolic concentrations of pyruvate in mammalian cells, but it also monitored glycolytic pyruvate production and mitochondrial pyruvate consumption.

4.1.4. Genetically encoded lactate sensors. A genetically encoded lactate sensor called Laconic was constructed by inserting the *E. coli* transcription factor LldR into a FRET pair (mTFP/Venus) (63). Laconic has two apparent K_d values of ∼8 μM and ∼830 μM and can detect lactate from 1 μM to 10 mM. Notably, the sensor's response to lactate was significantly interfered by pyruvate or citrate at high concentrations (63). In addition, Laconic has a very small dynamic range (∼10%), making it difficult to measure subtle lactate changes under physiological conditions. The Laconic sensor has been applied to monitor lactate metabolism in different mammalian cells (63).

4.2. Genetically Encoded Fluorescent Sensors for the Tricarboxylic Acid Cycle

For the TCA cycle, there are currently four types of genetically encoded fluorescent sensors available: the citrate sensors of the CIT family; the α-KG sensors OGsor, mOGsor, P_{II}-TC3, and P_{II}-TC3-R9P; the glutamine sensors Gln (D157N), Gln (D157N/T70A), and FLIPQ-TV3.0 family; and the glutamate sensors FLIPE, SuperGluSnFR, iGluSnFR, $iGlu_f$, $iGlu_u$, and R-iGluSnFR1 and R^{ncp}-iGluSnFR1 (**Table 1**).

4.2.1. Genetically encoded citrate sensors. A series of genetically encoded citrate sensors were engineered by inserting the citrate-binding domain of the *Klebsiella pneumoniae* histidine sensor kinase CitA into a FRET pair (CFP/Venus) (64). Citrate sensors have six typical variants (CIT8μ, CIT32μ, CIT50μ, CIT96μ, CIT0.5m, and CIT1.8m), whose K_d for glucose ranges from ∼8 μM to ∼1.765 mM in vitro. Upon citrate binding, the ratios of CIT sensors change by 20–55%. Notably, these sensors are barely functional at low pH, making the application of acidic compartments (i.e., endosomes or lysosomes) difficult. In addition, the citrate sensor can respond to high concentrations of isocitrate (>1 mM). Using citrate sensors, Ewald et al. (64) monitored the metabolic response of *E. coli* to different carbon substrates.

4.2.2. Genetically encoded α-ketoglutarate sensors. A series of genetically encoded α-KG sensors called OGsor were designed by inserting the α-KG-binding domain GAF of the NifA protein between the FRET pair YFP/CFP (65). These sensors respond to α-KG between 100 μM and 10 mM, with K_d values for α-KG between ∼0.4 mM and ∼2.0 mM in vitro, and exhibit a maximum change in fluorescence of 10–40%. Furthermore, an improved single-wavelength α-KG sensor, mOGsor, which was constructed by inserting the α-KG-binding domain GAF of the NifA protein into YFP, showed a larger dynamic range (150%) and better selectivity (66). Another genetically encoded α-KG sensor, P_{II}-TC3, was developed by inserting the signal transduction protein P_{II} from *Synechococcus elongatus* PCC 7942 between the FRET pair mCerulean/mVenus (67). The P_{II}-TC3 sensor and its variant P_{II}-TC3-R9P can detect α-KG from 0.1 μM to 0.1 mM and 10 μM to 10 mM, with a K_d for α-KG of ∼3 μM and ∼91 μM, respectively. With these sensors, intracellular-free α-KG levels were estimated to be 100–150 μM in living *E. coli* cells (67).

4.2.3. Genetically encoded glutamine sensors. A FRET-based sensor for glutamine was developed by inserting bacterial glutamine-binding protein from *E. coli* between ECFP and EYFP (68). The glutamine sensor Gln (D157N) or Gln (D157N/T70A) has a K_d of ∼6.9 mM or 18.8 mM, with a maximum change in fluorescence of 30–50%. The FLIPQ-TV3.0 family improved FRET-based glutamine sensors by inserting the *E. coli* glutamine-binding protein glnH between mTFP1 and Venus (69). FLIPQ-TV3.0 sensors have five variants (FLIPQ-TV3.0_R75K, _R75M, _D157N, _R75MY86A, and _R75MW220A), with K_d values for glutamine of 1.5 μM, 50 μM, 130 μM, 1.6 mM, and 7.6 mM, respectively. Cellular glutamine levels are predicted to be 1–22 mM (69); thus, the R75MY86A and R75MW220A mutants are more suitable for physiological glutamine detection. Notably, these two sensors have a small dynamic range (∼13%), which considerably decreases with increases in pH, especially in the physiological pH range (pH 7.0–8.0), making them barely applicable to alkaline mitochondria (pH 8.0). Utilizing these sensors, Gruenwald et al. (69) demonstrated that glutamine transporter activity can easily be monitored at the single-cell level.

4.2.4. Genetically encoded glutamate sensors. A genetically encoded glutamate sensor FLIPE was created by inserting the *E. coli* glutamate-binding protein GltI (also known as ybeJ)

between ECFP and Venus (70). FLIPE sensors have four variants (FLIPE-600n, FLIPE-10μ, FLIPE-100μ, and FLIPE-1m), with a K_d for glutamate of 600 nM, 10 μM, 100 μM, and 1.0 mM, respectively. Compared to other mutants, FLIPE-600n with a maximum ratio change of 27% is more suitable for the detection of glutamate release from neurons; however, this sensor exhibits obvious nonspecificity to aspartate, glutamine, and asparagine (70), making it difficult to measure cellular glutamate. The FRET-based glutamate sensor SuperGluSnFR can be improved by inserting the *E. coli* glutamate-binding protein ybeJ between ECFP and citrine (71, 72). SuperGluSnFR exhibits a 44% change in emission ratio upon glutamate binding with a K_d of 2.5 μM when expressed on the extracellular surface of neurons, a 6.2-fold improvement over the 7.1% average of original GluSnFR (71).

To optimize response magnitude, Marvin et al. (73) developed an intensity-based glutamate sensor (iGluSnFR) by fusing *E. coli* GltI with cpGFP, with a dynamic range of 450%. The purified iGluSnFR sensor indicated a K_d of ~107 μM for glutamate in vitro; however, the in situ affinity (K_d) of the sensor on HEK293 cells was ~4 μM, a 25-fold increase in affinity from that of the purified protein (73). Notably, the iGluSnFR sensor sensitively responds to aspartate, with a K_d of ~145 μM and a dynamic range of 200%. To improve the response kinetics of iGluSnFR, Helassa et al. (74) recently developed two faster variants ($iGlu_f$ and $iGlu_u$) with comparable brightness but increased K_d for glutamate (137 μM and 600 μM, respectively). iGluSnFR can specifically, sensitively, and rapidly respond to glutamate in situ and be used to work robustly for long-term imaging in somata, dendrites and spines in the retina, worms, zebrafish, and mice. To expand the palette of the sensor, Wu et al. (75) recently developed red intensity-based glutamate sensors (R-iGluSnFR1 and R^{ncp}-iGluSnFR1) based on iGluSnFR. R-iGluSnFR1 exhibits a dynamic range of ~490% and a glutamate affinity (K_d) of ~11 μM, and R^{ncp}-iGluSnFR1 exhibits a glutamate affinity (K_d) of ~0.9 μM while maintaining an ~480% dynamic range. Compared with iGluSnFR, R-iGluSnFR1 can reliably resolve action potential–evoked glutamate transients by electrical field stimuli in cultures of dissociated hippocampal neurons.

4.3. Genetically Encoded Fluorescent Sensors for Pyridine Dinucleotide

For pyridine dinucleotides, there are currently five types of genetically encoded fluorescent sensors available: the NADH sensor Frex; the NAD^+ sensor LigA-cpVenus; the NAD^+/NADH ratio sensors Peredox, RexYFP, and SoNar; the NADPH sensors of the iNap family; and the $NADP^+$ sensors Apollo-$NADP^+$ and NADPsor (**Table 1**).

4.3.1. Genetically encoded NADH sensors. The genetically encoded NADH sensor called Frex was engineered by inserting Rex from *Bacillus subtilis* (B-Rex) into cpYFP (76). Frex exhibits high selectivity and high responsiveness to NADH, with a dynamic range of 800%. Frex binds NADH with a K_d of approximately 3.7 μM and 11 μM at pH 7.4 and 8.0, respectively; thus, it is useful for measuring NADH levels ranging from 0.15 μM to 90 μM (77). Notably, Frex's response to NADH is not substantially affected by physiologic concentrations of free NAD^+ (78), making it an authentic NADH sensor rather than the NAD^+/NADH ratio sensor. As with other cpYFP-based sensors, Frex sensors are sensitive to pH fluctuations (76). In addition, Frex sensors are also limited by fluorescence signals, which are often 10 times lower than cpYFP's in various difficult-to-transfect cells (i.e., primary cells). This drawback may be explained by the poor folding of the mesophilic B-Rex protein and the low stability caused from the fusion and mutation of B-Rex in the engineering of Frex sensors (77). Based on Frex sensors, the cytosolic and mitochondrial-free NADH levels were estimated to be approximately 120 nM and 30 μM, respectively (76). We further found that the dynamic changes in NADH levels in subcellular organelles were affected by

NADH transport, glucose metabolism, electron transport chain function, and redox environment and demonstrated that cytosolic NADH is sensitive to environmental changes, while mitochondria have a strong tendency to maintain physiological NADH homeostasis (76).

4.3.2. Genetically encoded NAD^+ sensors. A genetically encoded NAD^+ sensor was developed by fusing cpVenus and the NAD^+-binding DNA ligase from bacteria (LigA) (abbreviated as LigA-cpVenus) (79). LigA-cpVenus exhibits a reversible response to NAD^+ and has no apparent response to other nucleotides (79). Upon NAD^+ binding, the fluorescence of LigA-cpVenus excited at 488 nm caused decreases of 50%, whereas the fluorescence intensity of LigA-cpVenus by 405-nm excitation remained unchanged; thus, it can be a ratiometric tool for measuring NAD^+ dynamics. This breakthrough has provided a novel tool for the determination of NAD^+ dynamics in living cells; however, the small dynamic range of LigA-cpVenus may limit its applications. As with other cpFP-based sensors, the LigA-cpVenus sensor is also sensitive to physiological pH flux (pH 6.0–8.0) (79). Based on LigA-cpVenus, the cytosolic, nuclear, and mitochondrial-free NAD^+ levels in HEK293T cells were estimated to be approximately 106 μM, 109 μM, and 230 μM, respectively. The authors further used the sensor to demonstrate that mitochondrial NAD^+ in HEK293T cells has multiple sources and that cytosolic NAD^+ may be transported into mitochondria (79).

4.3.3. Genetically encoded NAD^+/NADH ratio sensors. The NAD^+/NADH ratio biosensor Peredox was constructed by inserting cpT-sapphire between the two subunits of the thermophilic Rex from *Thermus aquaticus* (T-Rex) (80). Peredox sensitively responds to NADH; however, the fluorescence response of Peredox for NADH is lowered with increased NAD^+ concentration due to the competitive binding (80). Thus, Peredox reports the NAD^+/NADH ratio rather than the NADH level. Unfortunately, the fluorescence response of Peredox is not strictly dependent on the NAD^+/NADH ratio, given that a threefold change in the NAD^+ pool size in the physiologic range produced a twofold change in the sensor midpoint for the NAD^+/NADH ratio (80). Peredox has a 150% dynamic range, which is much smaller than that of Frex and SoNar sensors. Peredox has a high affinity for NADH with a $K_{NAD^+/NADH}$ of 330, making it easily saturated under normal cell culture conditions with glucose supplementation. This property of high affinity also slows down Peredox's fluorescence response when the NADH level decreases (81). Peredox has only one excitation peak and one emission peak and is an intensity-based sensor. To achieve a ratiometric measurement, the Peredox sensor is fused with the red fluorescent protein mCherry, which increases the molecular size of the sensor; it is also prone to aggregation of the fusion protein in mammalian cells (80). Using the Peredox sensor, Hung et al. (80) observed that primary astrocytes had a significantly lower cytosolic NAD^+/NADH ratio than primary neurons. Furthermore, high-content image analysis showed that cytosolic NADH in mammary epithelial MCF-10A cells decreased upon phosphatidylinositol-3-kinase (PI3K) pathway inhibition.

Another NAD^+/NADH ratio biosensor, RexYFP, is constructed by inserting cpYFP into the loop of T-Rex (82). RexYFP binds NADH with a K_d of ~0.18 μM and a dynamic range of 50%. In addition, RexYFP can also bind NADPH with a dissociation constant of 6.2 μM; thus, NADPH interfered with RexYFP's response to NADH at physiologic concentration. Similar to Peredox, RexYFP is also an intensiometric sensor with a single excitation peak at 490 nm and a single emission peak at 518 nm. Similar to Frex, cpYFP-based RexYFP is sensitive to pH fluctuation under physiological conditions.

The first-generation NADH sensors (Frex, Peredox, and RexYFP) all have certain weaknesses, such as weak fluorescence, high affinity, small dynamic range, or nonspecificity. To fill the current technical gap, we have developed a second-generation NAD^+/NADH sensor, SoNar, which

has many desirable properties for an ideal sensor, such as intense fluorescence, rapid response, high specificity, and large dynamic range (81). SoNar was created by inserting cpYFP between residues 189 and 190 of the T-Rex monomer lacking the DNA-binding domain using a short polypeptide linker (81). SoNar is an intrinsically ratiometric sensor with two excitation wavelengths (420 nm and 485 nm), and it responds to NADH and NAD^+ with opposing changes in fluorescence ratio. SoNar has an apparent K_d of 0.2 μM for NADH and 5 μM for NAD^+. Importantly, SoNar is strictly responsive to the NAD^+/NADH ratio in the presence of both NADH and NAD^+, regardless of the total concentration of NAD^+ or NADH. SoNar has an appropriate apparent $K_{NAD^+/NADH}$ of ≈40, making it useful to report either an increase or decrease of the cellular NAD^+/NADH ratio under different conditions. SoNar exhibits a 1,500% dynamic range under different NAD^+/NADH ratios, almost twofold greater than that of Frex, tenfold greater than that of Peredox, and 30-fold greater than that of RexYFP. Thus, it is one of the most responsive genetically encoded sensors currently available and enables better real-time tracking of the subtle differences of cellular metabolic states. Based on its superior properties, SoNar has been successfully applied in different research areas, including high-throughput metabolic screening (78, 81), quantification of the NAD^+/NADH ratio in different mammalian cells (20, 78, 81, 83–85), multiparametric imaging (35, 86), and in vivo imaging (20, 78, 81).

4.3.4. Genetically encoded NADPH sensors. Based on the highly responsive SoNar sensor, a series of genetically encoded NADPH sensors (iNap) were designed by engineering SoNar's binding site to switch ligand selectivity from NADH to NADPH (86). The iNap sensors are intrinsically ratiometric with two excitation wavelengths and have opposing responses to NADPH binding when excited at 420 nm and 485 nm, leading to ratiometric fluorescence changes of 500–1,000%. iNap fluorescence excited at 485 nm is sensitive to pH; however, its fluorescence excited at 420 nm is pH resistant. Thus, fusion of iNap and the red fluorescent protein mCherry allows ratiometric and pH-resistant measurement. NADPH sensors iNap 1–4 have different affinities with K_d values of ∼2.0 μM, ∼6.0 μM, ∼25 μM, and ∼120 μM, respectively, which further expand their applications in different cells and subcellular organelles. Notably, the response of iNap sensors to various NADPH concentrations is not substantially affected by physiological concentrations of free $NADP^+$, suggesting that $NADP^+$ does not compete with NADPH binding to iNap (86). Therefore, iNap can be used only as an authentic reporter for NADPH. iNap sensors have inherited superior properties from SoNar, including intense fluorescence, rapid responsiveness, pH insensitivity, and a wide dynamic range for ratiometric imaging in single living cells and in vivo (86). Utilizing iNap sensors, we found that the cytosolic-free NADPH level (∼3.1 μM) in mammalian cells was one order of magnitude higher than the free NADH level (∼0.12 μM). By contrast, the mitochondrion-free NADPH concentration (∼37 μM) was estimated to be roughly equal to the free NADH concentration (∼30 μM) previously measured by the Frex sensor (76). Thus, the mitochondrial NADPH pool deserves more attention, especially in the NAD(P)H autofluorescence assay, as it makes a comparable contribution to mitochondrial NAD(P)H signals. We further demonstrated that mammalian cells have a strong tendency to maintain physiological NADPH homeostasis, which is regulated by glucose-6-phosphate dehydrogenase and AMP kinase (86).

4.3.5. Genetically encoded $NADP^+$ sensors. A series of $NADP^+$ sensors of different colors, named Apollo-$NADP^+$ sensors, were designed by fusing single FPs and enzymatically inactive glucose-6-phosphate dehydrogenase (G6PD) (87). Apollo-$NADP^+$ sensors are based on the $NADP^+$-induced homodimerization of G6PD and were measured by the fluorescence anisotropy-based ratio of the parallel and perpendicular emission intensity with polarized light excitation.

Apollo-NADP$^+$ sensors keep a similar sensitivity to wild-type G6PD (K_d values of 0.1–20 μM) and exhibit specific, reversible, and rapid responses to NADP$^+$. Notably, the sensors are not pH sensitive within the pH range of 7.25–8. The weakness of Apollo-NADP$^+$ sensors is that they have a small dynamic range (15–20%) relative to other single FP sensors; their dynamic ranges may be further reduced by hetero-oligomerization of Apollo-NADP$^+$ sensors with the endogenous G6PD enzyme. In practice, the fluorescence response of the Apollo-NADP$^+$ sensors in live cells under oxidative stress may be 5% or less, making it technically difficult to use these sensors to measure subtle changes under physiologic conditions. For Apollo-NADP$^+$ sensors, the imaging of steady-state fluorescence anisotropy is heavily dependent on sophisticated instrumentation, which is not readily available in most laboratories. Cameron et al. (87) used Apollo-NADP$^+$ to study beta cells responding to oxidative stress and demonstrated that NADPH was significantly depleted before H_2O_2 accumulation by simultaneously imaging Apollo-NADP$^+$ with the H_2O_2 sensor HyPer.

Another genetically encoded NADP$^+$ sensor (NADPsor) was constructed by inserting NADP$^+$-binding ketopantoate reductase (KPR) into the FRET pair [CFP and YFP (88)]. The FRET-based sensor responds to NADP$^+$ but not to other derivatives; however, its dynamic range is only ∼30%. To improve the affinity, NADPsor is optimized in the binding pocket of KPR by means of computational protein redesign. Unfortunately, this sensor's response to NADP$^+$ is still insensitive, with a K_d of 2 mM for NADP$^+$, which can hardly be used to measure NADP$^+$ under physiological conditions.

4.4. Genetically Encoded Fluorescent Sensors for Energy Currency

For energy currency, there are currently four types of genetically encoded fluorescent sensors available: the ATP sensors of the ATeam group, AT1.03NL, and iATPSnFRs; the ADP sensor ADPrime; the ATP/ADP ratio sensors Perceval and PercevalHR; and the GTP sensors GEVALs (**Table 1**).

4.4.1. Genetically encoded ATP sensors. A series of FRET-based ATP sensor ATeams were generated by inserting *Bacillus subtilis* F_0F_1-ATP synthase between mseCFP and mVenus (89). ATeam has four variants (AT3.10, AT3.10^{MGK}, AT1.03^{YEMK}, and AT1.03), whose K_d for ATP ranges from 7.4 μM to 3.3 mM. The affinity of ATeam depends considerably on the temperature, with a fivefold increase from an elevation of 10°C. A modified version called AT1.03NL was reported to improve the performance of AT1.03 at relatively low temperatures (20–30°C) (90). AT1.03NL detects ATP dynamics more sensitively than the original AT1.03 in *Drosophila melanogaster* and *Caenorhabditis elegans*, which are typically cultured between 20°C and 25°C. Upon ATP binding, the fluorescence ratio of AT1.03 increases by ∼150%. Notably, the sensor was pH resistant within the pH range of 7.5–8; however, its dynamic range became smaller with the decreased pH. ATeam sensors respond rapidly and have been used for studying the bioenergetics of cancer cells (91) and the chemical screening of immunogenic cell death (92). Recently, single-wavelength ATP sensors (iATPSnFRs) were developed by insertion of circularly permuted superfolder GFP (cpSFGFP) into the epsilon subunit of F_0F_1-ATPase from *Bacillus PS3* (93). iATPSnFRs had a high specificity to ATP but sensitively responded to pH fluctuations. iATPSnFR had two variants, iATPSnFR$^{1.0}$ and iATPSnFR$^{1.1}$, with a dynamic range of ∼240% and ∼190%, respectively. iATPSnFRs had an ATP affinity (K_d) of approximately 50–120 μM, which is far lower than that of ATeam. Thus, iATPSnFRs are more suitable for the detection of cell surface ATP in mammalian cells.

4.4.2. Genetically encoded ADP sensors. The genetically encoded ADP sensor ADPrime was generated by inserting a bacterial ADP-binding protein between CFP and YFP (94). ADPrime showed a high affinity for ADP with an apparent K_d of ~0.16 μM and a dynamic range of ~8%. Notably, ADPrime also sensitively responded to ATP, with an apparent K_d of ~9.9 μM and a dynamic range of ~8%. The characteristic made it difficult for the detection of cell-surface ADP release or cellular ADP dynamics. Thus, an ADP sensor of superior performance remains highly desirable.

4.4.3. Genetically encoded ATP/ADP ratio sensors. The genetically encoded ATP/ADP ratio sensor Perceval was constructed by inserting cpmVenus into an ATP-binding bacterial protein GlnK1 (95). Perceval specifically responded to the ATP/ADP ratio with an apparent half-maximal signal change (K_R) of ~0.5 and a dynamic range of ~80%. Mammalian ATP/ADP ratios are expected to range from 1 to >100 under healthy conditions (96); thus, Perceval may be mostly saturated and does not sense a higher ATP/ADP ratio. PercevalHR (96) is an improved version of Perceval (95) with a similar design. PercevalHR has a dynamic range of 400%, almost fivefold greater than that of Perceval. More importantly, the ATP/ADP ratio at which PercevalHR shows K_R is ~3.5, which is nearly sevenfold larger than that of Perceval. PercevalHR covers a reliable detection range of 0.4 to 40, which is better matched to the physiological ATP/ADP ratio. PercevalHR has been used to visualize the association between the cellular energy state and the opening of K^+ channels (96) and to study the influence of axonal mitochondrial transport on the cellular energy state in neurons (97).

4.4.4. Genetically encoded GTP sensors. The genetically encoded GTP sensors GEVALs were developed by inserting cpYFP into a region of the bacterial G protein FeoB (98). GEVALs specifically bind to GTP but not to other related nucleotides. Five variants in the GEVAL family have various affinity to GTP, with K_d values ranging from 33 μM to 2.3 mM. GEVAL530 and GEVAL1150 are appropriate for GTP monitoring in living cells, as their affinities (K_d 528 μM and 1.13 mM) match well with the intracellular GTP concentration of 1–3 mM. These sensors show a dynamic response between 90% and 130%. Bianchi-Smiraglia et al. (98) demonstrated that the sensors responded well to the decrease or increase in GTP levels in live mammalian cells and were also suitable for high-throughput screening.

5. CONCLUSION AND OUTLOOK

Genetically encoded fluorescent sensors offer a powerful tool for monitoring live-cell or in vivo metabolite dynamics with high spatiotemporal resolution; therefore, they provide good alternatives to traditional biochemical methods. They can be applied for tracking or quantifying metabolites at the single-cell level, subcellular level, and even the in vivo level (**Figure 4*a*,*b***). For example, the subcellular NADH level, NAD^+ level, NAD^+/NADH ratio, and NADPH level have been quantified by Frex, LigA-cpVenus, SoNar, Peredox, and iNap sensors. More importantly, the NAD^+/NADH redox state has also been measured in living mice with the SoNar sensor. Although various biosensors have been developed, very few genetically encoded sensors can be used for in vivo studies, particularly in mammalian models. To our knowledge, none of the previously reported metabolite sensors has been reported in mammalian studies. Mitochondria are generally considered as the cellular energy factory, but live-cell imaging with ATeam showed that there is less ATP in mitochondria than in cytosol. In addition, genetically encoded metabolite sensors are valuable tools for the systematic analysis of regulatory networks affecting metabolite dynamics, i.e., uptake, efflux, and metabolism. We reported the rapid uptake

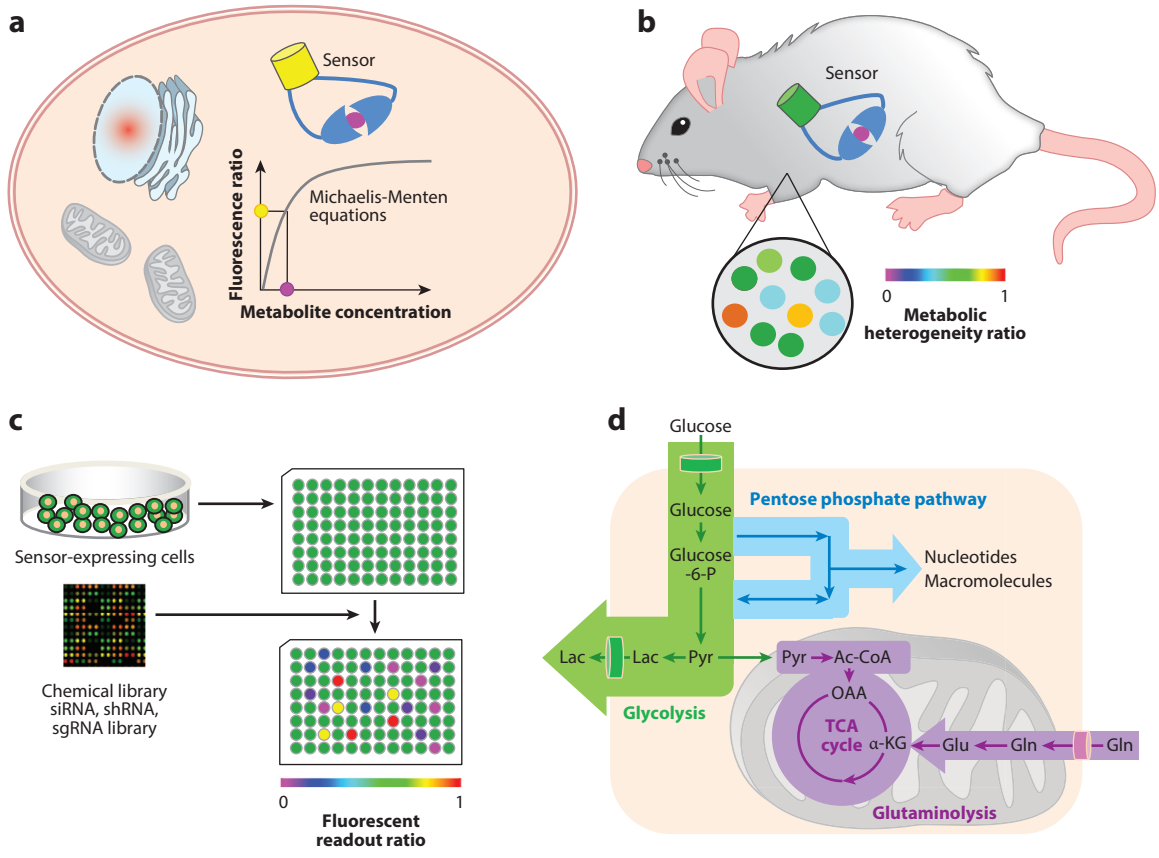

Figure 4

Typical applications of genetically encoded metabolite sensors. (*a*) Single-cell or subcellular metabolite imaging. (*b*) In vivo metabolite imaging. (*c*) High-throughput metabolic screen. (*d*) The delineation of live-cell metabolic phenomics. Abbreviations: Ac-CoA, acetyl-CoA; α-KG, α-ketoglutarate; Gln, glutamine; Glu, glutamate; Glucose-6-P, glucose-6-phosphate; Lac, lactate; OAA, oxaloacetate; Pyr, pyruvate; sgRNA, single guide RNA; shRNA, short hairpin RNA; siRNA, small interfering RNA; TCA, tricarboxylic acid.

of extracellular NADH across the plasma membrane of HEK293 cells with the Frex sensor (76), and Cambronne et al. (79) found that cytosolic NAD^+ might transport into mitochondria with the LigA-cpVenus sensor. In addition, a few sensors have also been utilized in metabolic screens (**Figure 4*c***), including $FLII^{12}Pglu\text{-}700\mu\delta6$ for genetic screens and SoNar for chemical screens. Utilizing the SoNar sensor, we examined the effect of >5,500 compounds on cell metabolism and identified KP372-1 as a potent redox cycling antitumor agent (81).

Despite the exciting progress made by research on metabolite biosensors, several key challenges undoubtedly lie ahead. First, most metabolite sensors in central carbon metabolism are lacking, such as glucose-6-phosphate, glyceraldehyde-3-phosphate, and phosphoenolpyruvate in glycolysis, and acetyl-CoA, isocitrate, succinate, malate and oxaloacetate in the TCA cycle. More importantly, none of the metabolite sensors were reported in the pentose phosphate pathway. In the future, the development of these metabolite sensors will enrich our methodological toolbox and will be very useful for the delineation of live-cell metabolic phenomics, which consists of strategies to quantitatively monitor cellular or subcellular metabolites and to understand how

trafficking of these biochemical messengers through the metabolic network influences live-cell phenotype (**Figure 4*d***). Second, even less numerous are existing sensors with good performance. The sensors for NAD^+/NADH, NADPH, ATP, ATP/ADP, glutamate, and glucose show large dynamic range and appropriate affinity in practical application; however, there is a pressing need for the optimization of sensors for pyruvate, lactate, citrate, α-KG, glutamine, NAD^+, $NADP^+$, and ADP owing to their small dynamic change, inappropriate affinity, poor specificity, or complicated measurement among other factors. Thus, superior sensors for these metabolites are still highly desired and remain to be developed. Third, almost all existing sensors are limited to a single green or yellow hue, and sensors with a broad spectrum of colors are urgently needed. Sensors with distinct hues allow us to perform the multiparametric analysis of metabolites in live cells. For example, the multiplex imaging of glycolysis and the pentose phosphate pathway in the same cell will greatly enhance our understanding of the regulation of metabolic fates of glucose. Because of their barrel-like rigid structure, most FPs are difficult to engineer for the circular permutation forms, which presents a great challenge in engineering multicolor FP sensors. Therefore, there is an urgent need to improve existing FPs or to search for novel FPs or mimics. Finally, although genetically encoded fluorescent sensors are endowed with the unique advantages of in situ imaging, metabolomics and metabolic flux analysis can shed light on global metabolite profiling and metabolic networks, and nuclear magnetic resonance may invasively record multiple metabolites at one time. Thus, the combined use of these technologies will paint the landscape of cell metabolism and provide the paramount view of metabolic regulation.

DISCLOSURE STATEMENT

The authors are not aware of any affiliations, memberships, funding, or financial holdings that might be perceived as affecting the objectivity of this review.

ACKNOWLEDGMENTS

This research is supported by the National Key Research and Development Program of China (grants 2019YFA0904800, 2017YFA050400, 2017YFC0906900), National Natural Science Foundation of China (grants 91649123, 31722033, 31671484, 91857202, 21937004, 31601119), the Shanghai Science and Technology Commission (grants 18JC1411900, 16430723100), Research Unit of New Techniques for Live-Cell Metabolic Imaging (Chinese Academy of Medical Sciences, grant 2019RU01), Major Program of Development Fund for Shanghai Zhangjiang National Innovation Demonstration Zone (Stem Cell Strategic Biobank and Stem Cell Clinical Technology Transformation Platform, grant ZJ2018-ZD-004), the innovative research team of high-level local universities in Shanghai, Young Elite Scientists Sponsorship Program by CAST, Shanghai Young Top-Notch Talent Program, the State Key Laboratory of Bioreactor Engineering, and the Fundamental Research Funds for the Central Universities.

LITERATURE CITED

1. Shyh-Chang N, Daley GQ, Cantley LC. 2013. Stem cell metabolism in tissue development and aging. *Development* 140:2535–47
2. Lopez-Otin C, Blasco MA, Partridge L, Serrano M, Kroemer G. 2013. The hallmarks of aging. *Cell* 153:1194–217
3. Ghesquiere B, Wong BW, Kuchnio A, Carmeliet P. 2014. Metabolism of stromal and immune cells in health and disease. *Nature* 511:167–76
4. Buck MD, Sowell RT, Kaech SM, Pearce EL. 2017. Metabolic instruction of immunity. *Cell* 169:570–86

5. Mergenthaler P, Lindauer U, Dienel GA, Meisel A. 2013. Sugar for the brain: the role of glucose in physiological and pathological brain function. *Trends Neurosci.* 36:587–97
6. Kasischke KA, Vishwasrao HD, Fisher PJ, Zipfel WR, Webb WW. 2004. Neural activity triggers neuronal oxidative metabolism followed by astrocytic glycolysis. *Science* 305:99–103
7. Shapses SA, Sukumar D. 2012. Bone metabolism in obesity and weight loss. *Annu. Rev. Nutr.* 32:287–309
8. Am. Diabetes Assoc. 2002. Evidence-based nutrition principles and recommendations for the treatment and prevention of diabetes and related complications. *Diabetes Care* 25:202–12
9. Yuan HX, Xiong Y, Guan KL. 2013. Nutrient sensing, metabolism, and cell growth control. *Mol. Cell* 49:379–87
10. Boroughs LK, DeBerardinis RJ. 2015. Metabolic pathways promoting cancer cell survival and growth. *Nat. Cell Biol.* 17:351–59
11. Harris JJ, Jolivet R, Attwell D. 2012. Synaptic energy use and supply. *Neuron* 75:762–77
12. Possemato R, Marks KM, Shaul YD, Pacold ME, Kim D, et al. 2011. Functional genomics reveal that the serine synthesis pathway is essential in breast cancer. *Nature* 476:346–50
13. Patra KC, Hay N. 2014. The pentose phosphate pathway and cancer. *Trends Biochem. Sci.* 39:347–54
14. Suganuma T, Workman JL. 2018. Chromatin and metabolism. *Annu. Rev. Biochem.* 87:27–49
15. Mills E, O'Neill LA. 2014. Succinate: a metabolic signal in inflammation. *Trends Cell Biol.* 24:313–20
16. Dang L, White DW, Gross S, Bennett BD, Bittinger MA, et al. 2009. Cancer-associated IDH1 mutations produce 2-hydroxyglutarate. *Nature* 462:739–44
17. Toro JR, Nickerson ML, Wei MH, Warren MB, Glenn GM, et al. 2003. Mutations in the fumarate hydratase gene cause hereditary leiomyomatosis and renal cell cancer in families in North America. *Am. J. Hum. Genet.* 73:95–106
18. Altman BJ, Stine ZE, Dang CV. 2016. From Krebs to clinic: glutamine metabolism to cancer therapy. *Nat. Rev. Cancer* 16:619–34
19. Schild T, Low V, Blenis J, Gomes AP. 2018. Unique metabolic adaptations dictate distal organ-specific metastatic colonization. *Cancer Cell* 33:347–54
20. Hao X, Gu H, Chen C, Huang D, Zhao Y, et al. 2019. Metabolic imaging reveals a unique preference of symmetric cell division and homing of leukemia-initiating cells in an endosteal niche. *Cell Metab.* 29:950–65.e6
21. Zenobi R. 2013. Single-cell metabolomics: analytical and biological perspectives. *Science* 342:1243259
22. Lowry OH, Passonneau JV, Schulz DW, Rock MK. 1961. The measurement of pyridine nucleotides by enzymatic cycling. *J. Biol. Chem.* 236:2746–55
23. Zhao X, Jiang J, Yang G, Huang J, Yang G, et al. 2017. Profiling and preparation of metabolites from pyragrel in human urine by online solid-phase extraction coupled with high performance liquid chromatography tandem mass spectrometry followed by a macroporous resin-based purification approach. *Molecules* 22:494
24. Paglia G, Astarita G. 2017. Metabolomics and lipidomics using traveling-wave ion mobility mass spectrometry. *Nat. Protoc.* 12:797–813
25. Cai K, Haris M, Singh A, Kogan F, Greenberg JH, et al. 2012. Magnetic resonance imaging of glutamate. *Nat. Med.* 18:302–6
26. Li J, Vosegaard T, Guo Z. 2017. Applications of nuclear magnetic resonance in lipid analyses: an emerging powerful tool for lipidomics studies. *Prog. Lipid Res.* 68:37–56
27. Otieno AC, Mwongela SM. 2008. Capillary electrophoresis-based methods for the determination of lipids—a review. *Anal. Chim. Acta* 624:163–74
28. Britz-McKibbin P, Terabe S. 2003. On-line preconcentration strategies for trace analysis of metabolites by capillary electrophoresis. *J. Chromatogr. A* 1000:917–34
29. Gaglio D, Metallo CM, Gameiro PA, Hiller K, Danna LS, et al. 2011. Oncogenic K-Ras decouples glucose and glutamine metabolism to support cancer cell growth. *Mol. Syst. Biol.* 7:523
30. Canto C, Gerhart-Hines Z, Feige JN, Lagouge M, Noriega L, et al. 2009. AMPK regulates energy expenditure by modulating NAD^+ metabolism and SIRT1 activity. *Nature* 458:1056–60
31. Yang H, Yang T, Baur JA, Perez E, Matsui T, et al. 2007. Nutrient-sensitive mitochondrial NAD^+ levels dictate cell survival. *Cell* 130:1095–107

32. Hiller K, Metallo CM. 2013. Profiling metabolic networks to study cancer metabolism. *Curr. Opin. Biotechnol.* 24:60–68
33. Sun F, Dai C, Xie J, Hu X. 2012. Biochemical issues in estimation of cytosolic free NAD/NADH ratio. *PLOS ONE* 7:e34525
34. Maddocks OD, Labuschagne CF, Vousden KH. 2014. Localization of NADPH production: a wheel within a wheel. *Mol. Cell* 55:158–60
35. Zou Y, Wang A, Shi M, Chen X, Liu R, et al. 2018. Analysis of redox landscapes and dynamics in living cells and in vivo using genetically encoded fluorescent sensors. *Nat. Protoc.* 13:2362–86
36. Mayevsky A, Rogatsky GG. 2007. Mitochondrial function in vivo evaluated by NADH fluorescence: from animal models to human studies. *Am. J. Physiol. Cell Physiol.* 292:C615–40
37. Chance B, Cohen P, Jobsis F, Schoener B. 1962. Intracellular oxidation-reduction states in vivo. *Science* 137:499–508
38. Eto K, Tsubamoto Y, Terauchi Y, Sugiyama T, Kishimoto T, et al. 1999. Role of NADH shuttle system in glucose-induced activation of mitochondrial metabolism and insulin secretion. *Science* 283:981–85
39. Mayevsky A, Barbiro-Michaely E. 2009. Use of NADH fluorescence to determine mitochondrial function in vivo. *Int. J. Biochem. Cell Biol.* 41:1977–88
40. Blacker TS, Mann ZF, Gale JE, Ziegler M, Bain AJ, et al. 2014. Separating NADH and NADPH fluorescence in live cells and tissues using FLIM. *Nat. Commun.* 5:3936
41. Skala MC, Riching KM, Gendron-Fitzpatrick A, Eickhoff J, Eliceiri KW, et al. 2007. In vivo multiphoton microscopy of NADH and FAD redox states, fluorescence lifetimes, and cellular morphology in precancerous epithelia. *PNAS* 104:19494–99
42. Huang S, Heikal AA, Webb WW. 2002. Two-photon fluorescence spectroscopy and microscopy of NAD(P)H and flavoprotein. *Biophys. J.* 82:2811–25
43. Bartolome F, Abramov AY. 2015. Measurement of mitochondrial NADH and FAD autofluorescence in live cells. *Methods Mol. Biol.* 1264:263–70
44. Ghukasyan VV, Heikal AA, ed. 2014. *Natural Biomarkers for Cellular Metabolism: Biology, Techniques, and Applications*. Boca Raton, FL: CRC Press
45. Shaner NC, Steinbach PA, Tsien RY. 2005. A guide to choosing fluorescent proteins. *Nat. Methods* 2:905–9
46. Gross S, Piwnica-Worms D. 2005. Spying on cancer: molecular imaging in vivo with genetically encoded reporters. *Cancer Cell* 7:5–15
47. Frommer WB, Davidson MW, Campbell RE. 2009. Genetically encoded biosensors based on engineered fluorescent proteins. *Chem. Soc. Rev.* 38:2833–41
48. Knopfel T, Diez-Garcia J, Akemann W. 2006. Optical probing of neuronal circuit dynamics: genetically encoded versus classical fluorescent sensors. *Trends Neurosci.* 29:160–66
49. De Michele R, Carimi F, Frommer WB. 2014. Mitochondrial biosensors. *Int. J. Biochem. Cell Biol.* 48:39–44
50. Zhao Y, Yang Y. 2015. Profiling metabolic states with genetically encoded fluorescent biosensors for NADH. *Curr. Opin. Biotechnol.* 31C:86–92
51. Okumoto S. 2010. Imaging approach for monitoring cellular metabolites and ions using genetically encoded biosensors. *Curr. Opin. Biotechnol.* 21:45–54
52. Topell S, Hennecke J, Glockshuber R. 1999. Circularly permuted variants of the green fluorescent protein. *FEBS Lett.* 457:283–99
53. Nagai T, Sawano A, Park ES, Miyawaki A. 2001. Circularly permuted green fluorescent proteins engineered to sense Ca^{2+}. *PNAS* 98:3197–202
54. Baird GS, Zacharias DA, Tsien RY. 1999. Circular permutation and receptor insertion within green fluorescent proteins. *PNAS* 96:11241–46
55. Takanaga H, Chaudhuri B, Frommer WB. 2008. GLUT1 and GLUT9 as major contributors to glucose influx in HepG2 cells identified by a high sensitivity intramolecular FRET glucose sensor. *Biochim. Biophys. Acta* 1778:1091–99
56. Deuschle K, Okumoto S, Fehr M, Looger LL, Kozhukh L, Frommer WB. 2005. Construction and optimization of a family of genetically encoded metabolite sensors by semirational protein engineering. *Protein Sci.* 14:2304–14

57. Bermejo C, Haerizadeh F, Takanaga H, Chermak D, Frommer WB. 2011. Optical sensors for measuring dynamic changes of cytosolic metabolite levels in yeast. *Nat. Protoc.* 6:1806–17
58. Hou BH, Takanaga H, Grossmann G, Chen LQ, Qu XQ, et al. 2011. Optical sensors for monitoring dynamic changes of intracellular metabolite levels in mammalian cells. *Nat. Protoc.* 6:1818–33
59. Hu HY, Wei YF, Wang DC, Su N, Chen XJ, et al. 2018. Glucose monitoring in living cells with single fluorescent protein-based sensors. *RSC Adv*. 8:2485–89
60. Fehr M, Frommer WB, Lalonde S. 2002. Visualization of maltose uptake in living yeast cells by fluorescent nanosensors. *PNAS* 99:9846–51
61. Marvin JS, Schreiter ER, Echevarria IM, Looger LL. 2011. A genetically encoded, high-signal-to-noise maltose sensor. *Proteins* 79:3025–36
62. San Martín A, Ceballo S, Baeza-Lehnert F, Lerchundi R, Valdebenito R, et al. 2014. Imaging mitochondrial flux in single cells with a FRET sensor for pyruvate. *PLOS ONE* 9:e85780
63. San Martín A, Ceballo S, Ruminot I, Lerchundi R, Frommer WB, Barros LF. 2013. A genetically encoded FRET lactate sensor and its use to detect the Warburg effect in single cancer cells. *PLOS ONE* 8:e57712
64. Ewald JC, Reich S, Baumann S, Frommer WB, Zamboni N. 2011. Engineering genetically encoded nanosensors for real-time in vivo measurements of citrate concentrations. *PLOS ONE* 6:e28245
65. Zhang C, Wei ZH, Ye BC. 2013. Quantitative monitoring of 2-oxoglutarate in *Escherichia coli* cells by a fluorescence resonance energy transfer-based biosensor. *Appl. Microbiol. Biotechnol.* 97:8307–16
66. Zhang C, Ye BC. 2014. A single fluorescent protein-based sensor for in vivo 2-oxogluatarate detection in cell. *Biosens. Bioelectron*. 54:15–19
67. Lüddecke J, Francois L, Spät P, Watzer B, Chilczuk T, et al. 2017. P_{II} protein-derived FRET sensors for quantification and live-cell imaging of 2-oxoglutarate. *Sci. Rep.* 7:1437
68. Yang H, Bogner M, Stierhof YD, Ludewig U. 2010. H-independent glutamine transport in plant root tips. *PLOS ONE* 5:e8917
69. Gruenwald K, Holland JT, Stromberg V, Ahmad A, Watcharakichkorn D, Okumoto S. 2012. Visualization of glutamine transporter activities in living cells using genetically encoded glutamine sensors. *PLOS ONE* 7:e38591
70. Okumoto S, Looger LL, Micheva KD, Reimer RJ, Smith SJ, Frommer WB. 2005. Detection of glutamate release from neurons by genetically encoded surface-displayed FRET nanosensors. *PNAS* 102:8740–45
71. Hires SA, Zhu Y, Tsien RY. 2008. Optical measurement of synaptic glutamate spillover and reuptake by linker optimized glutamate-sensitive fluorescent reporters. *PNAS* 105:4411–16
72. Tsien RY. 2005. Building and breeding molecules to spy on cells and tumors. *FEBS Lett*. 579:927–32
73. Marvin JS, Borghuis BG, Tian L, Cichon J, Harnett MT, et al. 2013. An optimized fluorescent probe for visualizing glutamate neurotransmission. *Nat. Methods* 10:162–70
74. Helassa N, Durst CD, Coates C, Kerruth S, Arif U, et al. 2018. Ultrafast glutamate sensors resolve high-frequency release at Schaffer collateral synapses. *PNAS* 115:5594–99
75. Wu J, Abdelfattah AS, Zhou H, Ruangkittisakul A, Qian Y, et al. 2018. Genetically encoded glutamate indicators with altered color and topology. *ACS Chem. Biol.* 13:1832–37
76. Zhao Y, Jin J, Hu Q, Zhou HM, Yi J, et al. 2011. Genetically encoded fluorescent sensors for intracellular NADH detection. *Cell Metab*. 14:555–66
77. Zhao Y, Yang Y. 2016. Real-time and high-throughput analysis of mitochondrial metabolic states in living cells using genetically encoded NAD^+/NADH sensors. *Free Radic. Biol. Med.* 100:43–52
78. Zhao Y, Wang A, Zou Y, Su N, Loscalzo J, Yang Y. 2016. In vivo monitoring of cellular energy metabolism using SoNar, a highly responsive sensor for NAD^+/NADH redox state. *Nat. Protoc.* 11:1345–59
79. Cambronne XA, Stewart ML, Kim D, Jones-Brunette AM, Morgan RK, et al. 2016. Biosensor reveals multiple sources for mitochondrial NAD^+. *Science* 352:1474–77
80. Hung YP, Albeck JG, Tantama M, Yellen G. 2011. Imaging cytosolic NADH-NAD^+ redox state with a genetically encoded fluorescent biosensor. *Cell Metab*. 14:545–54
81. Zhao Y, Hu Q, Cheng F, Su N, Wang A, et al. 2015. SoNar, a highly responsive NAD^+/NADH sensor, allows high-throughput metabolic screening of anti-tumor agents. *Cell Metab*. 21:777–89
82. Bilan DS, Matlashov ME, Gorokhovatsky AY, Schultz C, Enikolopov G, Belousov VV. 2014. Genetically encoded fluorescent indicator for imaging NAD^+/NADH ratio changes in different cellular compartments. *Biochim. Biophys. Acta* 1840:951–57

83. Titov DV, Cracan V, Goodman RP, Peng J, Grabarek Z, Mootha VK. 2016. Complementation of mitochondrial electron transport chain by manipulation of the NAD^+/NADH ratio. *Science* 352:231–35
84. Oldham WM, Clish CB, Yang Y, Loscalzo J. 2015. Hypoxia-mediated increases in L-2-hydroxyglutarate coordinate the metabolic response to reductive stress. *Cell Metab.* 22:291–303
85. Kim W, Deik A, Gonzalez C, Gonzalez ME, Fu F, et al. 2019. Polyunsaturated fatty acid desaturation is a mechanism for glycolytic NAD^+ recycling. *Cell Metab.* 29:856–70
86. Tao R, Zhao Y, Chu H, Wang A, Zhu J, et al. 2017. Genetically encoded fluorescent sensors reveal dynamic regulation of NADPH metabolism. *Nat. Methods* 14:720–28
87. Cameron WD, Bui CV, Hutchinson A, Loppnau P, Graslund S, Rocheleau JV. 2016. Apollo-$NADP^+$: a spectrally tunable family of genetically encoded sensors for $NADP^+$. *Nat. Methods* 13:352–58
88. Zhao FL, Zhang C, Tang Y, Ye BC. 2016. A genetically encoded biosensor for in vitro and in vivo detection of $NADP^+$. *Biosens. Bioelectron.* 77:901–6
89. Imamura H, Nhat KP, Togawa H, Saito K, Iino R, et al. 2009. Visualization of ATP levels inside single living cells with fluorescence resonance energy transfer-based genetically encoded indicators. *PNAS* 106:15651–56
90. Tsuyama T, Kishikawa J, Han YW, Harada Y, Tsubouchi A, et al. 2013. In vivo fluorescent adenosine 5′-triphosphate (ATP) imaging of *Drosophila melanogaster* and *Caenorhabditis elegans* by using a genetically encoded fluorescent ATP biosensor optimized for low temperatures. *Anal. Chem.* 85:7889–96
91. Roesch A, Vultur A, Bogeski I, Wang H, Zimmermann KM, et al. 2013. Overcoming intrinsic multidrug resistance in melanoma by blocking the mitochondrial respiratory chain of slow-cycling $JARID1B^{high}$ cells. *Cancer Cell* 23:811–25
92. Menger L, Vacchelli E, Adjemian S, Martins I, Ma Y, et al. 2012. Cardiac glycosides exert anticancer effects by inducing immunogenic cell death. *Sci. Transl. Med.* 4:143ra99
93. Lobas MA, Tao R, Nagai J, Kronschläger MT, Borden PM, et al. 2019. A genetically encoded single-wavelength sensor for imaging cytosolic and cell surface ATP. *Nat. Commun.* 10:711
94. Trull KJ, Miller P, Tat K, Varney SA, Conley JM, Tantama M. 2019. Detection of osmotic shock-induced extracellular nucleotide release with a genetically encoded fluorescent sensor of ADP and ATP. *Sensors* 19:3253
95. Berg J, Hung YP, Yellen G. 2009. A genetically encoded fluorescent reporter of ATP:ADP ratio. *Nat. Methods* 6:161–66
96. Tantama M, Martinez-Francois JR, Mongeon R, Yellen G. 2013. Imaging energy status in live cells with a fluorescent biosensor of the intracellular ATP-to-ADP ratio. *Nat. Commun.* 4:2550
97. Zhou B, Yu P, Lin MY, Sun T, Chen Y, Sheng ZH. 2016. Facilitation of axon regeneration by enhancing mitochondrial transport and rescuing energy deficits. *J. Cell Biol.* 214:103–19
98. Bianchi-Smiraglia A, Rana MS, Foley CE, Paul LM, Lipchick BC, et al. 2017. Internally ratiometric fluorescent sensors for evaluation of intracellular GTP levels and distribution. *Nat. Methods* 14:1003–9